TONAL NOISE PREDICTION OF SERRATED TRAILING-EDGE AIRFOILS

Yehia Salamav *[1], Basim Al Tluav †[2], and Johana Rocha ‡[2]
[1]Department of Mechanical and Aerospace Engineering, Carleton University, Ottawa, Ontario.

Résumé

Dans ce travail, des simulations intégrées de grandes turbulences sont utilisées en association avec le modèle Ffowcs Williams-Hawkings pour prédire les pics sonores des voilures NACA0012 ayant différentes configurations de bord de fuite anti-bruit. Différentes configurations de dentelure en dents de scie de plaques non plates sont étudiées et des essais expérimentaux en soufflerie sont réalisés. Les résultats sont validés puis comparés aux mesures expérimentales, et un accord qualitatif est obtenu en termes de statistiques d'écoulement et de spectres de bruit en champ lointain. Il est démontré que les dentelures en dents de scie TE modifient considérablement l'aérodynamique du sillage et améliorent le mélange à travers le profil aérodynamique. Les résultats expérimentaux confirment que les dentelures en dents de scie réduisent le bruit à large bande émis par le profilé au détriment de la génération d'un pic tonal, causé par le délestage tourbillonnaire associé à l'émoussement des extrémités de la dentelure. Des dentelures plus longues et des valeurs plus élevées d'émoussement des extrémités sont responsables de la force des tourbillons rejetés et de l'intensité du bruit tonal rayonné. La fréquence à laquelle les pics tonaux se produisent peut être contrôlée pour la même amplitude de dentelure et le même émoussement de l'extrémité de la dentelure, en modifiant la longueur d'onde. Des valeurs de longueur d'onde plus élevées pour une même amplitude de dentelure et un même émoussage de l'extrémité de la dentelure conduisent à des pics de fréquence tonale plus élevés, et des valeurs d'émoussage de l'extrémité de la dentelure plus élevées pour une même amplitude de dentelure et une même longueur d'onde conduisent à des pics de fréquence tonale plus bas accompagnés d'amplitudes de crête plus élevées.

Mots clefs : embedded large eddy simulation; bruits de bord de fuite; dentelures de bord de fuite, airfoil, soufflerie

Abstract

In this work, Embedded Large Eddy Simulations are employed in tandem with the Ffowcs Williams-Hawkings model to predict the tonal peaks of NACA0012 airfoils having different noise-suppressing trailing-edge configurations. Different non-flat plate sawtooth serration configurations are investigated and experimental wind tunnel testing is performed. Results are validated then compared with experimental measurements, and qualitative agreement is obtained in terms of flow statistics and the far-field noise spectra. TE sawtooth serrations are shown to significantly modify the aerodynamics of the wake and improve mixing across the airfoil. Experimental results confirm that sawtooth serrations reduce the broadband noise radiated by the airfoil at the expense of generating a tonal peak, caused by vortex shedding associated with the bluntness of the serration roots. Longer serrations, and higher values of root bluntness are responsible for the strength of the shed vortices and the intensity of the radiated tonal noise. The frequency at which the tonal peaks occur can be controlled for the same serration amplitude and root bluntness by modifying the wavelength. Larger wavelength values for the same serration amplitude and root bluntness lead to higher tonal peak frequencies, and larger values of root bluntness for the same serration amplitude and wavelength lead to lower tonal peak frequencies accompanied by higher peak amplitudes.

Keywords: embedded large eddy simulation; trailing-edge noise; trailing edge serration, airfoil, wind tunnel

1 Introduction

With the world growing increasingly noisier, aerodynamic noise reduction has been steadily gaining the attention of the research community. Over the past few decades, noise pollution has increased, disturbing the integrity of natural ecosystems and putting them at risk [1]. Humans are suffering from noise pollution as it impacts their quality of life and puts their mental and physical well-being at risk [2].

In parallel, global warming has led a universal push towards sustainability, promoting an increased interest in renewable power sources to replace coal and fossil fuels, and reduce greenhouse gas emissions. One of these sustainable resources is to harness the energy of wind through wind turbines. Despite their many advantages, the noise produced by such turbines is still of the most significant hindrance preventing their widespread use, and the largest contributor to this noise pollution is that generated by the trailing edge of wind turbine blades [3]. For those reasons, TE noise reduction has become a crucial challenge in many industrial sectors.

To investigate the possibility of having low-noise airfoils, researchers and engineers turned to nature, and in 1934, R. R. Graham [4] was the first to recognize the potential of using birds as a reference to render modern airplanes more efficient, and specifically identified owls as a biomim-

* Yehia.Salama@cmail.carleton.ca
† Basim.AlTlua@cmail.carleton.ca
‡ Joana.Rocha@carleton.ca

icry candidate to achieve silent flight. The wings of owls differ from those of all other groups of birds. Three main noise reduction peculiarities were observed in owl wings, which distinguish them from other birds:

- the leading-edge comb: A remarkably stiff comb-like fringe exists on the front margin of every feather.
- the trailing-edge fringe: A fringe resembling that of a shawl spans along the TE of the main wing.
- the downy upper surface: Certain parts of the upper surface are covered with a short, fine down.

Soon afterwards, more researchers followed the same path and were drawn to nature looking for inspiration. In 1998, Lilley [5] confirmed the three main noise suppression mechanisms in owl wings previously addressed by Graham [4]. The author then discussed the aerodynamic characteristics of each of these devices and proposed explanations as to how the flow dynamics vary, leading to large noise reduction in the range of frequencies above 2 kHz. According to him:

- the comb-shaped leading-edge feathers behave as closely spaced co-rotating vortex generators creating streamwise vortices which lead to a reduction in boundary layer (BL) thickness and in the volume of turbulence crossing the TE.
- the trailing-edge fringe resembles a serrated edge which suggests the reduction or even elimination of TE scattering.
- given the small diameter of its fibers, the compliant velvety surface of the wing acts as a bypass mechanism for energy dissipation at frequencies smaller than the conventional dissipation range of frequencies associated with viscous damping. In other words, the fibers absorb energy from the small-scale noise-emitting eddies, thus silencing them.

Following the work of these authors, further work has been using the owl as a biomimicry model. The proceeding step was to implement owl wing features in a practical way on solid airfoils to study their efficiency as noise suppressers and their effect on aerodynamic flow properties. Extensive experimental work has been conducted to confirm the applicability of TE extensions, serrations in particular, as noise suppression devices [6-9]. Chong et al. [8] experimentally investigated the feasibility of employing different serrated TE configurations to reduce the noise produced by a NACA0012 airfoil. For the case of an untripped boundary layer, testing velocities of up to 60 m/s and an angle of attack of 4.2°, it was shown that sound power reduction of up to 30 dB is possible for the instability tonal noise. When the airfoil surface is tripped, broadband sound power reduction of 6.5 dB was achieved. However, more significant narrowband noise is generated by the vortex shedding at the serration roots. The authors concluded even though smaller serration angles lead to better broadband noise reduction, larger angles are recommended to account for the unavoidable narrowband vortex shedding noise.

Numerical simulations were used to predict far-field noise radiation. In 2000, Manoha, Troff and Sagaut [10] successfully predicted the far-field noise generated by turbulence flowing over the blunt TE of a thick flat plate by coupling a Large Eddy Simulation (LES) with Curle's solution to the Lighthill equation, then the Ffowcs-Williams and Hawkings (FW-H) analogy. Agrawal et and Sharma [11] also assessed the effectiveness of biomimicry in reducing aerodynamic noise using LES. The interaction between the wake of a cylindrical rod and a downstream airfoil was simulated to investigate the effect of sinusoidal leading-edge serrations on radiated noise. Tang et al. [12] performed simulations employing LES using the Lighthill-Curle method in an attempt to reveal the variation in the hydrodynamic field and sound source associated with TE serrations on a NACA 0012 airfoil. It was confirmed that TE serrations reduce the radiated noise seeing that serrations impede the growth of spanwise vortices, i.e. decrease spanwise coherence, and promote streamwise ones near the wake. Zilstra and Johnson [13] demonstrated the ability of LES, combined with the FW-H acoustic analogy, to predict the flow field and acoustic results for a SD7037 airfoil at a Re of 43,000 and different angles of attack. Overall, the method proved to be an effective airfoil self-noise prediction tool at static angles of attack (AOAs).

Despite the increase in computing power over the last two decades, Large Eddy Simulations remain prohibitively expensive. Because of the impracticality of LES and the need for reliable short-response-time noise prediction methods for industrial design and optimization, some researchers resorted to statistical models based on steady RANS solutions in a sequential CFD/CAA approach. Markus [14] reviewed three different methods based on steady Reynolds-averaged Navier-Stokes (RANS) solutions to predict noise emitted from airfoils [15-17]. Validation studies showed decent agreement between the considered methods and results from experiments, a semi-empirical airfoil self-noise prediction code and LES. In another attempt to get accurate noise predictions at a reasonable computational cost, Quéméré and Sagaut [18] presented a novel zonal multi-domain RANS/LES method (also known as Embedded LES or ELES), where the full domain configuration was decomposed into several subdomains that can be treated with either RANS or LES. The same concept was later adopted by Teraccol [19], who investigated using ELES to represent aerodynamic noise sources. The method was applied to a flat plate with a blunt TE and a NACA0012 airfoil. In this approach, zonal LES is only performed close to the main elements responsible for sound generation, while the overall configuration is treated by a RANS. The most critical point was the numerical treatment performed at the inlet of the LES domain. CPU time reductions in the order of 40 were obtained and the method was found to be an attractive compromise between accuracy and computational cost. In 2008, Fröhlich and von Terzi [20] presented a generic review of the various ELES approaches along with different interface treatment strategies. The review provided information on how to distinguish between the different methods and to further the understanding of their inherent limitations as well as the encountered difficulties. Successful simulation results demonstrated the high potential of the approach. In the same year, Mathey [21] evaluated using the ELES approach for the prediction of broadband and tonal noise gen-

erated by the flow past an airfoil TE at a high Re. Two simulations were performed for a free stream velocity of 30.5 m/s and a chord based Re of 1,800,000. The first one used a random forcing method at the RANS/LES interface, and the second one used the Vortex Method. The far-field noise was calculated using the FW-H model. The results showed that the technique is capable of capturing the separated flow and reproducing the main characteristics of the aeroacoustic sources. Lastly, it was shown that the use of the Vortex Method (VM) for the generation of a synthetically turbulent flow field significantly improved the accuracy of the simulation. Kim et at. [22] used a segregated ELES approach to predict the aeroacoustic and aerodynamic properties of several flatback airfoils at high Re and compared the results to semi-empirical and experimental data. Synthetic turbulence was generated at the RANS/LES interface using the Vortex Method and far-field acoustics were computed using the FW-H analogy. The obtained frequency spectra of surface pressure fluctuations obtained is in good agreement with experimental measurements at the same observer location and the hybrid RANS-LES method is found to be adequate for predicting aerodynamic noise generation by vortical flow in the vicinity of a blunt TE airfoil over a range of frequencies. Lane, Croaker and Ding [23] tested and implemented ELES for the prediction of TE noise due to flow around a NACA 0012 airfoil. The obtained results were compared to a full LES simulation and to experimental data. Both simulations used the same mesh resolution and the same wall-modeled LES approach. For ELES, the mesh size was only about 13 million cells, compared to 40 million cells for the full LES. It was found that the results of both simulations were in good agreement. The ELES approach resulted in saving 55% of the computational cost of a full LES. Zuo et al. [24] performed flow simulations using ELES to analyze the aerodynamic and noise characteristics of a serrated-TE NACA0018 airfoil at a Re of 160,000 and an AOA of 6 degrees. Two airfoils having the same serration wave length and different serration amplitudes were considered and compared to a plain straight TE case. Predictions based on the FW-H acoustic analogy showed that longer serrations are more effective in decreasing the overall sound pressure levels.

In the present work, ELES is adopted to study the flow field around a flat-TE NACA0012 airfoil as well as three serrated-TE airfoils having different serration amplitudes and wavelengths, at zero AOA. The far-field noise is computed using the Ffowcs Williams–Hawkings (FW-H) model and attention is given to the tonal peaks generated by the serrated airfoils. The flow chord-based Reynold's number, Re_c, is approximately 500,000. The computational results are validated and compared with available experimental data. The used ELES configuration, where the LES region only partially covers the airfoil chord-length, hasn't been used to investigate bio-inspired TE designs yet. In this context, the main goals of this study are to provide a faster alternative to the currently-used computationally prohibitive simulation models and use it to visualize the flow field around TE serrations, as well as assess the effect of changing different serration parameters on the radiated tonal noise.

This paper is structured as follows. Section 2 presents the numerical methodology with the governing LES equations (Sec. 2.1), Section 2.2 describes the hybrid RANS/LES interface treatment and Section 2.3 presents the FW-H aeroacoustic analogy. Thereafter, Section 3 describes the flow configuration (Sec. 3.1), the computational mesh (Sec. 3.2) and the experimental setup (Sec. 3.3). All results are presented in Sec. 4.

2 Numerical methods

2.1 Governing equations

The governing equations used in the current study, termed the spatially-filtered Na-vier-Stokes equations, are obtained by applying a low pass filter on the time dependent Navier-Stokes equations in the physical space. The flow is assumed incompressible. In order to increase efficiency, the filter width is the same size as the mesh spacing used in the computational domain. The resulting equations describe the dynamics of large eddies [25, 26]. Field variables, such as pressure and velocity, are defined by their convolution with a filter function over the fluid domain:

$$\bar{\phi}(x) = \int_D \phi(x')G(x,x')dx' \; ; \tag{1}$$

where D is the fluid domain and G is the filtering function. The overbar indicates spatial filtering and not temporal averaging. After applying the filter to the mass and momentum conservation equations, the NS equations become:

$$\frac{\partial \rho}{\partial t} + \frac{\partial}{\partial x_i}(\rho \overline{u}_i) = 0, \tag{2}$$

$$\frac{\partial}{\partial t}(\rho \overline{u}_i) + \frac{\partial}{\partial x_j}(\rho \overline{u}_i \overline{u}_j) = \frac{\partial}{\partial x_j}(\sigma_{ij}) - \frac{\partial \overline{p}}{\partial x_i} - \frac{\partial \tau_{ij}}{\partial x_j}. \tag{3}$$

In order to obtain a close system of equations, the unknown SGS stresses are modeled by applying the Boussinesq eddy viscosity hypothesis [27], thus computing the sub-grid-scale turbulent stresses from

$$\tau_{ij} - \frac{1}{3}\tau_{kk}\delta_{ij} = -2\,\mu_t \overline{S}_{ij} \; ; \tag{4}$$

where μ_t is the subgrid-scale turbulent viscosity and τ_{kk} is the isotropic part of the SGS. The latter part is not modeled as it is added to the filtered static pressure term. S_{ij} is the strain-rate tensor of the resolved scale calculated from equation (5) using the filtered velocity components :

$$\overline{S}_{ij} = \frac{1}{2}\left(\frac{\partial \overline{u_i}}{\partial x_j} + \frac{\partial \overline{u_j}}{\partial x_i}\right) \tag{5}$$

For the Wall Adapting Local Eddy Viscosity (WALE) model [28], μ_t is modeled as:

$$\mu_t = \rho L_s^2 \frac{\left(S_{ij}^d S_{ij}^d\right)^{\frac{3}{2}}}{\left(\overline{S_{ij}}\,\overline{S_{ij}}\right)^{\frac{5}{2}} + \left(S_{ij}^d S_{ij}^d\right)^{\frac{5}{4}}} \; ; \tag{6}$$

where L_s, the mixing length of the sub-grid scale, and S_{ij}^d, which is a function of the strain and rotation rate tensors, are defined in equations (7) and (8) as:

$$L_s = \min\left(\kappa d, C_w V^{\frac{1}{3}}\right), \tag{7}$$

$$S_{ij}^d = \frac{1}{2}\left(\overline{g}_{ij}^2 + \overline{g}_{ji}^2\right) - \frac{1}{3}\delta_{ij}\overline{g}_{kk}^2 ; \tag{8}$$

and g_{ij} is defined in equation (9) as :

$$\overline{g}_{ij} = \frac{\partial \overline{u}_i}{\partial x_j}. \tag{9}$$

In equation (7), d is the distance to the closest wall, V is the volume of the computational cell, κ = 0.41 is the von Kármán constant and C_w = 0.325 is the WALE constant.

2.2 RANS/LES Interface

In the present approach, the entire flow domain is decomposed into clearly identifiable regions for RANS and LES before the simulation is started. This is usually referred to as segregated modeling. The goal is to use each model where it is best suited. The flow is initialized using RANS equations, which provide stationary field statistics, and LES re-solves the unsteady high-resolution perturbations near the TE, where it is needed. The main difficulty is defining proper interface conditions, seeing that inappropriate coupling could lead to results contamination in the LES or RANS subdomains.

At the inflow interface, mass, momentum and energy are convected into the LES subdomain from the RANS region. The latter provides mean values which are to be coupled with the LES data. To obtain correct LES results, fluctuations must be provided at the interface and added to the mean flow computed by RANS. These fluctuations can be real, provided by precursor simulations or databases of similar flows, or synthetic, provided by Fourier modes, digital filters, random vortices...etc. The goal is to make the imposed fluc-tuation as close as possible to those present in a real physical flow.

The Vortex Method [29] was chosen as a means of adding artificial resolved turbulence at the RANS/LES interface. In this approach, a fluctuating vorticity field is added to the mean flow, consequently creating perturbations similar in behavior to realistic ones. The VM is based on the Biot-Savart law and the 2D evolution equation of vorticity. Vortex points, or particles, are distributed over the inlet interface perpendicular to the streamwise direction and are randomly convected, carrying information about the vorticity field. The amount of vorticity carried by a given particle "i" is represented by the circulation Γ according to equation (11), and the assumed spatial distribution is given by equation (12), such that:

$$\omega(\vec{x}, t) = \sum_{i=1}^{N} \Gamma_i(t)\, \eta(|\vec{x} - \vec{x}_i|, t)\,, \tag{10}$$

$$\Gamma_i(x, y) = 4\sqrt{\left(\frac{\pi A k(x, y)}{3N(2\ln(3) - 3\ln(2))}\right)}\,; \tag{11}$$

$$\eta(\vec{x}) = \frac{1}{2\pi\sigma^2}\left(2e^{\frac{-|x|^2}{2\sigma^2}} - 1\right)2e^{\frac{-|x|^2}{2\sigma^2}}; \tag{12}$$

where N is the number of vortex points, A is the inlet section area, k is the turbulence kinetic energy and σ controls the size of the vortex particles. The resulting discretization for the velocity field is given by:

$$\vec{u}(\vec{x}) = \frac{1}{2\pi}\sum_{i=1}^{N}\Gamma_i\frac{\left((\vec{x_i} - \vec{x}) \times \vec{z}\right)}{\left|\vec{x} - \vec{x_i}'\right|^2}\left(1 - e^{\frac{\left|\vec{x}-\vec{x}'\right|^2}{2\sigma^2}}\right)e^{-\frac{\left|\vec{x}-\vec{x}'\right|^2}{2\sigma^2}}\,; \tag{13}$$

where $\vec{z}$ is a unit vector in the streamwise direction and x_i is the location of the i-th vortex particle. The value of σ is calculated from a known profile of mean turbulence kinetic energy and mean dissipation rate at the inlet, such that:

$$\sigma = \frac{ck^{3/2}}{2\epsilon}\,; \tag{14}$$

where c = 0.16. The minimum value of σ is determined by the local mesh size to ensure that the vortices will always belong to the resolved scale. Furthermore, the sign of the circulation of each vortex is randomly changed every characteristic time scale, which is the time needed for a 2D vortex to travel n times its mean characteristic 2D size in the boundary normal direction, where n is set to equal 100 from numerical testing. Finally, a rescaling model is used, and the velocity fluctuations are expressed as:

$$u_i'^{*} = u_i'\frac{\sqrt{< u_i u_i >}}{\sqrt{\frac{2}{3k}}}\,; \tag{15}$$

where $u_i'^{*}$and u_i' are the scaled and unscaled velocity fluctuations, and $< u_i u_i >$ represents the normal statistic velocity fluctuations.

2.3 The FW-H aeroacoustic analogy

To overcome the prohibitive cost of directly resolving the pressure fluctuations responsible for noise in the far-field, a method based on Lighthill's acoustic analogy [30] is used. In this approach, the nearfield flow is computed using the appropriate governing equations of ELES, and the far-field noise is predicted with the aid of an analytically de-rived integral solution to the wave equation. The acoustic analogy decouples sound generation from its propagation, thus allowing the separation of the flow solution from the acoustic analysis and the extraction of acoustic sources from the CFD domain.

The Ffowcs Williams and Hawkings (FW-H) formulation [31] adopts the most gen-eral form of Lighthill's acoustic analogy. The FW-H equation [31, 32] is nothing but an in-homogeneous wave equation derived by manipulating the continuity and Navier-Stokes equation. The FW-H equation can be expressed as:

$$\begin{aligned}\frac{1}{a_\infty^2}\frac{\partial^2 p'}{\partial t^2} - \nabla^2 p' = {} & \frac{\partial}{\partial t}\{[\rho_\infty v_n + \rho(u_n - v_n)]\delta(f)\} \\ & - \frac{\partial}{\partial x_i}\{[P_{ij} + \rho u_i(u_n - v_n)]\delta(f)\} \\ & + \frac{\partial^2}{\partial x_i \partial x_j}\{T_{ij}H(f)\},\end{aligned} \tag{16}$$

$$T_{ij} = \rho u_i u_j + P_{ij} - a_\infty^2(\rho - \rho_\infty)\delta_{ij}\,; \quad (17)$$

where $p' = p - p_\infty$ is the sound pressure at the far-field, u_i is the fluid velocity component in the x_i direction, u_n is the velocity component normal to the surface $f = 0$, v_i is the surface velocity component in the x_i direction, v_n is the surface velocity component normal to the surface, $\delta(f)$ is the Dirac delta function and $H(f)$ is the Heaviside function. The subscript "∞" denotes free-stream parameters. The $f = 0$ surface is a mathematical surface representing the source surface. n_i is a unit vector normal pointing towards the exterior region of the source (f>0), a_∞ is the speed of the sound at the far field, T_{ij} is the Lighthill stress tensor defined in equation (17) P_{ij} is the compressive stress tensor. The first term on the RHS of equation (16) represents the monopole or thickness source, modeling the sound generated by the displacement of a fluid as a body passes through it. The second term is the dipole or loading source, resulting from the unsteadiness of the forces acting on the body's surface. The third term is the quadrupole source term, representing the non-linear fluctuations in the local sound speed and fluid velocity near the body surface. Monopole and dipole sources are dominant in low Mach number flows. By integrating equation (16) assuming free-space flow and no obstacles between the sound source and receiver, a full solution consisting of surface and volume integrals is obtained [32]. In the present case, the volume integral is neglected as it is only significant in high Mach number flows. Thus, the far-field sound pressure can be expressed as :

$$p'(\vec{x},t) = p'_T(\vec{x},t) + p'_L(\vec{x},t) \quad (18)$$

where:

$$4\pi p'_T(x,t) = \int_{f=0}\left[\frac{\rho_\infty(\dot{U_n} + \dot{U_n})}{r(1-M_r)^2}\right]dS + \int_{f=0}\left[\frac{\rho_\infty U_n\{r\dot{M}_r + a_\infty(M_r - M^2)\}}{r^2(1-M_r)^3}\right]dS \quad (19)$$

$$4\pi p'_T(x,t) = \frac{1}{a_\infty}\int_{f=0}\left[\frac{\dot{L_r}}{r(1-M_r)^2}\right]dS + \int_{f=0}\left[\frac{L_r - L_M}{r^2(1-M_r)^2}\right]dS + \frac{1}{a_\infty}\int_{f=0}\left[\frac{L_r\{r\dot{M}_r + a_\infty(M_r - M^2)\}}{r^2(1-M_r)^3}\right]dS \quad (20)$$

$$U_i = v_i + \frac{\rho}{\rho_\infty}(u_i - v_i) \quad (21)$$

$$L_i = P_{ij}\,\hat{n_j} + \rho u_i(u_n - v_n) \quad (22)$$

A dot over a variable indicates the source-time derivative of that variable, while the subscripts "n", "r" and "M" denote the dot product with the unit normal vector, the unit radiation vector and surface velocity vector normalized by the speed of sound, respectively.

3 Flow configuration and computational setup

3.1 Flow configuration

The airfoil selected for the present study is a NACA0012 symmetric airfoil to isolate the effect of lift generation on the radiated noise. The chord length of the airfoils c is $0.3\ m$. The airfoil is placed in a square $10c \times 10c$ domain. The flow domain is divided into two regions as seen in figure 1. RANS equations are employed in a coarse RANS domain, while LES equations are employed in a refined LES region near the TE. It's important to note that only the noise radiated by the flow within the LES region is predicted in the numerical simulations. Since the presented work is focused on TE noise predictions, it is reasonable to neglect the noise generated by other airfoil sections, such as the leading edge. All airfoil geometric parameters are shown in table 1. s is the span of the flow domain. Two embedded configurations were tested. For cases C1.1 and C1.2, the LES domains in the streamwise direction extend from $x/c = 0.5$ and $x/c = 0.7$, respectively, to $1c$ downstream of the TE. The letter "C' stands for computational. The origin is defined at the airfoil leading edge. In the transverse direction, the LES domain extends $0.25c$ above and below the airfoil. Two serration configurations are also tested. A general model of the serration characteristics is presented in figure 2. Table 2 summarizes the flow parameters of the simulations. Computations are carried out at a free stream velocity $u_\infty = 24$ m/s and a free stream Mach number $M_\infty = 0.071$, resulting in a chord-based Reynolds number, $Re_c = \rho u_\infty D/\mu$, of approximately $500{,}000$, where ρ is the fluid density, μ is the dynamic viscosity and D is the characteristic length, which is the airfoil chord in this case.

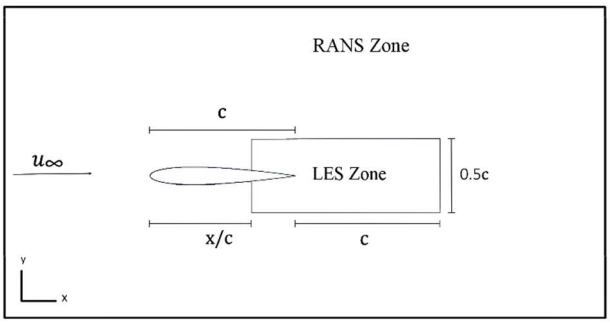

Figure 1: Schematic illustration of the segregated modeling domains.

Table 1: Geometric parameters of simulated aifoils.

Case	c [mm]	s [mm]	$2h$ [mm]	λ [mm]	ϵ [mm]
C1.1	300	18	–	–	–
C1.2	300	30	–	–	–
C2.1	300	30	30	10	7.4
C2.2	300	30	60	7.5	16.3
C2.3	300	30	60	10	16.3

Table 2: Flow parameters.

u_∞	24 m/s
M_∞	0.071
Re_c	500,000
μ	$1.7894 * 10^{-5}$ kg/m/s
ρ	1.225 kg/m^3
AOA	0

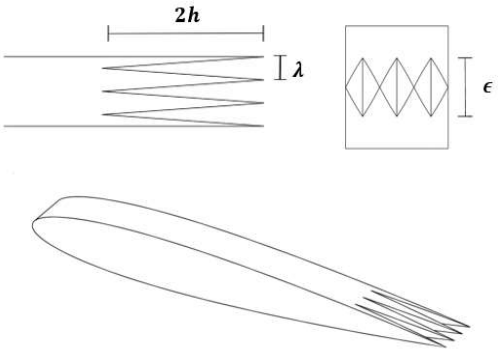

Figure 2: General serration configuration, not to scale.

3.2 Computational mesh and setup

A predominantly hexahedral mesh is generated following the cartesian cut-cell method (figure 3). This meshing technique, which has received a significant development in recent years [33]**Erreur ! Source du renvoi introuvable.**, was found ideal for the current study seeing that it results in a smaller number of elements for the same resolution compared to other methods, thus significantly reducing the simulation time. In addition, the resulting elements are characterized by their high orthogonal quality and low skewness, which minimizes truncation errors [33, 34]. Element size is restricted to 25.6 mm in the coarse RANS zone, 0.8 mm in the refined LES zone and 0.2 mm on the airfoil surface in the vicinity of the TE. Elements in the airfoil wake of the RANS zone have a size of 5 mm. The grid resolution in terms of wall-normal units is defined by:

$$\Delta x^+ = \frac{u_\tau \Delta x}{\nu}, \Delta y^+ = \frac{u_\tau \Delta y}{\nu} \text{ and } \Delta z^+ = \frac{u_\tau \Delta z}{\nu},$$

where u_τ is the frictional velocity and ν is the kinematic viscosity. 40 inflation layers (figure 3c) are generated around the airfoil with the thickness of the first layer set to $7.6 * 10^{-3}$ mm and a growth factor of 1.08, thus ensuring $y^+ < 0.5$ everywhere on the airfoil surface (figure 4), at least 3 layers in the viscous sublayer and overall accurate boundary layer resolution. Table 3 lists mesh statistics for all simulated cases. The chosen computational grid has a maximum resolution $\Delta x^+_{max} \leq 20$ and $\Delta z^+_{max} \leq 20$ in the streamwise and spanwise directions, respectively [35, 36]. Case C2.3 is simulated using two different meshes to investigate the effect of the mesh on the predicted tonal peak. A steady-state mesh convergence study was carried out by

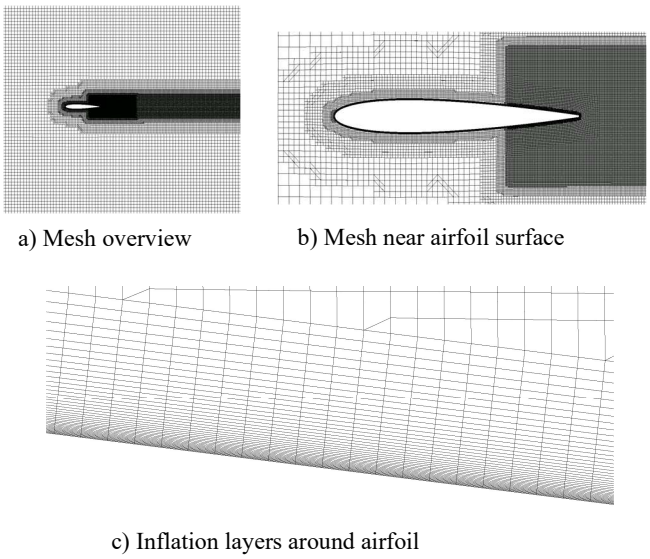

a) Mesh overview b) Mesh near airfoil surface

c) Inflation layers around airfoil

Figure 3: Computational mesh.

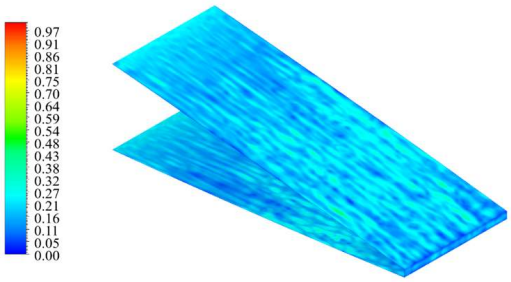

Figure 4: Instantaneous y^+ distribution.

Table 3: Mesh elements.

Case	RANS	LES	Total
C1.1	456,353	4,586,780	5,043,133
C1.2	976,300	5,690,368	6,666,668
C2.1	976,300	6,134,898	7,111,198
C2.2	976,300	5,896,422	6,872,722
C2.3, Mesh 1	976,300	5,647,833	6,624,133
C2.3, Mesh 2	1,050,433	6,173,725	7,224,158

progressively refining the mesh, creating three meshes having 6,666,668 elements, 7,606,083 elements and 9,011,531 elements respectively. The values of integrated output parameters, such as lift and drag coefficients, were compared and the maximum error is found to be less than 0.4%, demonstrating mesh convergence. Furthermore, the first two meshes were carried over for a transient simulation analysis. The lift-history coefficients were evaluated for each mesh at every time step and their RMS values were computed. Both meshes yield the same lift-coefficient RMS value, $c_{L_{RMS}} = 0.0013$. Consistent results in terms of integrated flow parameters, for both steady-state and transient simulations, are a

strong indication of the convergence of the used computational mesh, i.e. the mesh directly resolves enough flow structures for the results not to change with mesh refinement.

The boundary conditions used are demonstrated in figure 5. A velocity inlet boundary condition is specified at the domain entrance, where $u_\infty = 24$ m/s. Periodic boundary conditions (PBCs) are applied on the right and left side walls of the domain in the spanwise direction to allow the flow to develop naturally. No-slip boundary conditions are applied on the airfoil surface and a zero gauge-pressure outlet boundary condition is used. The inlet turbulence is set to 0.3%. The SIMPLE pressure-velocity coupling scheme is used. All results are second order accurate in time and space.

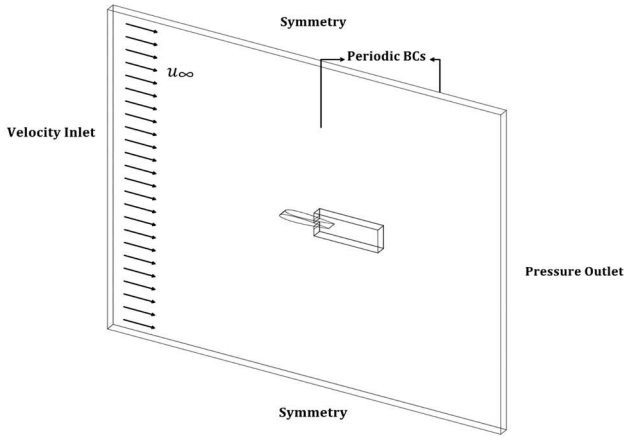

Figure 5: Boundary conditions.

The flow is initialized using the k-ω SST model developed by Menter [37], as it gives accurate separation predictions for external flows. The VM is then used to inject turbulence at the RANS/LES interface and the simulation is run for $4T_{TF}$ "Through-flow time" to obtain a fully developed flow, where $T_{TF} = L_{CFD}/u_\infty$ [36]. L_{CFD} is the LES domain length in the streamwise direction. WALE subgrid-scale (SGS) modelling is employed in the LES region as it is designed to return correct asymptotic wall behavior for wall-bounded flows [25]. The time step $\mathrm{d}t = 1.2 * 10^{-5}$ seconds. With these values, the Courant-Friedrichs-Lewy (CFL) number achieved is ≤ 1 everywhere in the domain, meaning the flow particles don't travel more than the length of one mesh element every time step. Residuals are reduced by three orders of magnitude each time step. Lastly, acoustic data is gathered for $3T_{TF}$. All convergence residuals are set to 10^{-5}. Pressure and velocity monitoring points were placed in the airfoil wake and statistical convergence is achieved. Statistical convergence is also achieved for the coefficients of lift and drag. All simulations are carried out using the commercial CFD software FLUENT 2019R3 and run on Intel Xeon L5410 2.33 GHz platform of 60 cores.

3.3 Experimental setup

Experiments were conducted in the medium-speed, subsonic, closed-loop wind tunnel at Carleton University (figure 6). The airflow is powered by a 37.3 kW (50 HP) variable-speed DC motor driving a 1.2 m axial propeller at speeds as high as 900 RPM. A variable frequency drive (VFD) modulates the rotational frequency of the fan at a resolution of 1.0 Hz. A series of turbulence grids precede a 9:1 contraction, which reduces the turbulence intensity levels in the center of the test section to less than 0.27%. The tunnel has a removable, rectangular test section along with the surrounding anechoic chambers was completed to be used for aeroacoustic testing. This test section is a 0.78 m × 0.51 m rectangular section, 1.83 m long. The upper and lower walls of the test section are each composed of two aluminum sheet panels and contain hardware (circle aluminum material) for the vertical mounting of a two-dimensional airfoil in the midway, and 0.45 m from the upstream end of the test section [38, 39].

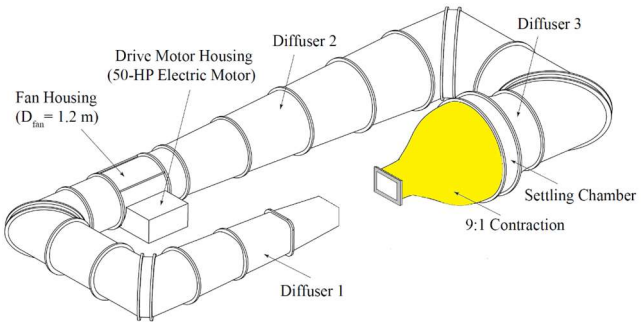

Figure 6: Wind tunnel configuration at Carleton University.

The airfoil wing is mounted vertically in the test section (figure 7) with its leading edge (at zero AOA) 0.45 m downstream of the test section entrance. The airfoil under investigation is a NACA0012 airfoil with a sawtooth TE serration cut directly into the main body of the airfoil (as shown in figure 8). The chord length of the airfoil is 300 mm, and the width is 510 mm. Between the leading-edge ($x/c = 0$), and $x/c = 0.73$ mm, the original NACA0012 airfoil profile is unmodified, where x is the streamwise direction. Further downstream, $0.73 \leq x/c \leq 1.0$, is a section that can be removed and replaced by either an unmodified or modified TE profile. Once attached, the TE section forms a continuous profile giving the appearance that the serrations are cut into the main body of the NACA0012 airfoil. Typical parameters including the serration amplitude, $2h$, and serration wavelength, λ, are defined as specified in figure 2. A prominent feature for airfoil that this type of serrated TE is the exposure of a significant bluntness ϵ at the root region. A photograph of the sawtooth serrated TEs used is shown in figure 8.

Table 4 shows the summary of geometrical parameters of the two TE serration tested in the present paper, according to $2h$, λ and ϵ, in which E0 represents the baseline sharp trailing-edge. The letter "E" stands for experimental. Far-field noise measurements in the mid-span were performed by a calibrated Brüel & Kjær microphone, which is installed at a distance of 1.4 m for an observer angle $\alpha = 90°$. The analysis was carried out between 100 Hz and 5 kHz.

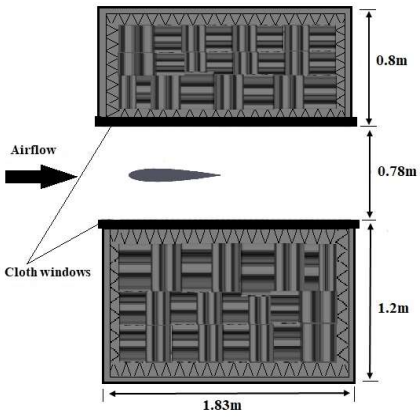

Figure 7: Cross section through the aeroacoustic test section and anechoic chamber as seen from above (top) and photograph of serrated-TE airfoil mounted in test section (bottom).

Figure 8: From left to right: NACA0012 main body, TE of case E0, TE of case E1 and TE of case E2.

Table 4: Geometric parameters of all experimental cases.

Case	c [mm]	s [mm]	$2h$ [mm]	λ [mm]	ϵ [mm]
E0	300	500	–	–	–
E1	300	500	70	25	18.2
E2	300	500	60	10	16.6

4 Results

4.1 Surface pressure

The pressure coefficient distribution around the airfoil is an important parameter, since it determines the lift coefficient and the development of the boundary layer [40-42]. In addition, the BL is responsible for the majority of the generated sound. C_p distributions for cases C1.1 and C1.2 are computed for validation and compared against experimental results obtained by Lee and Kang [43] for a NACA 0012 airfoil at a Re = 600,000, and full LES results published by Marsden, Bogey and Bailly [44] at $Re_c = 500{,}000$ (figure 9). Excellent agreement is found between the computational and experimental results. Of importance is the fact that from $x/c = 0.15$ down to the TE, the boundary layer is subject to an adverse pressure gradient. Both cases C1.1 and C1.2 are validated against existing literature. The LES domain in C1.1 is longer in the streamwise direction as it starts at a $x/c = 0.5$, while it starts at $x/c = 0.7$ in C1.2 (see tables 1 and 3). Even though both configurations yield acceptable results, the configuration of case C1.2 is chosen for the succeeding simulations as the LES domain covers a larger span.

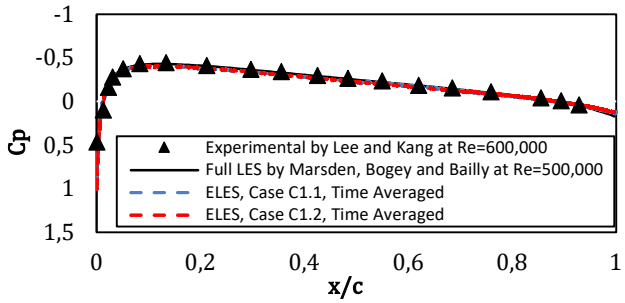

Figure 9: C_p distribution on airfoil surface.

Figure 10 shows the locations of maximum pressure fluctuation, where P_{RMS} is maximum for cases C1.2, C2.1, C2.2 and C2.3. For case C1.1, the location of maximum P_{RMS} is close to the sharp TE, seeing that that is where the discontinuity occurs and the BLs on the upper and lower sides clash. The introduction of serrations concentrated the maximum pressure fluctuation region from the extremity of the TE to downstream of the serration roots. This is where the pressure fluctuations are most violent, which suggests that aeroacoustic improvement to this design would require a modification of the flow field at that area, because regions with the highest P_{RMS} emit the most noise. The presence of serrations mitigates the sudden interaction between the BLs on the pressure and suction sides, thus allowing for progressive mixing and affecting the radiated sound. By comparing the maximum P_{RMS} values for C2.1, C2.2 and C2.3, the maximum P_{RMS} increases as the serration amplitude, and subsequently the root bluntness, are increased. C2.2 and C2.3 share the same root bluntness, ϵ, and serration amplitude, $2h$, and are subject to comparable P_{RMS} values.

4.2 Wake characteristics

By calculating the coefficient of lift, $c_L = L/(0.5 * \rho v^2 A)$, for every timestep of flow simulation, the lift-coefficient history can be plotted. L is defined as the lift force and A is the airfoil area. The lift-coefficient history is commonly used as an indicator of statistical convergence in transient simulations. Furthermore, it's a non-dimensional representation of the fluctuating forces acting normal to the airfoil surface due to the turbulence of air flow. To demonstrate the

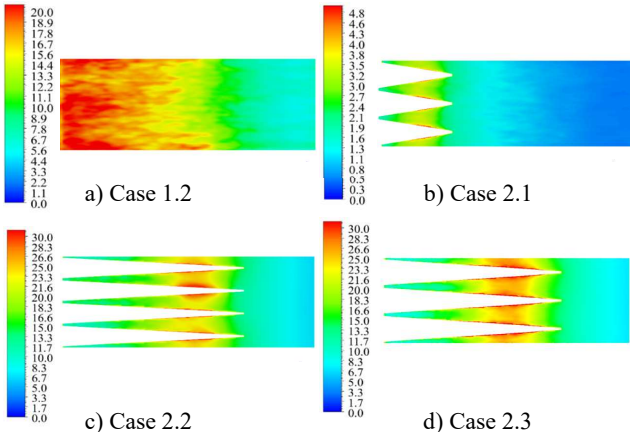

Figure 10: P_{RMS} distribution near airfoil TE.

convergence of the computational mesh, C2.3 is simulated twice, using two different meshes having 6,624,133 and 7,224,158 elements, respectively. The obtained lift-coefficient history plots are presented in figure 11. Both simulations yield the same lift-variation amplitude and frequency once the flow is initialized. The only observable difference is a phase shift, which is normal and simply means each simulation started from a different point in the periodic cycle. Both simulations also predict the same Strouhal number, $St = 0.168$. Figure 12 shows the lift-coefficient history plots of all the presented cases. All axes are kept constant and aligned for the sake of clarity and comparison. For case C1.2, the lift monitor is random and irregular, characterized by a relatively small amplitude. With the introduction of serrations, the lift monitors adopt sinusoidal shapes having different wavelengths and frequencies. C2.1 is characterized by the smallest amplitude and highest frequency, $f = 388$ Hz. C2.2 and C2.3 are almost subject to the same fluctuation amplitude, but their lift-coefficients vary with distinct frequencies equal to 218 Hz and 248 Hz, respectively. This behavior is attributed to the vortices shed in the wake of the airfoil. The dominant frequencies of the periodic plots were obtained by applying discrete Fast-Fourier Transform (FFT) on the propagated presented lift-coefficient history plots. Figure 13 shows the instantaneous flow fields in the airfoil wake in term of iso-surfaces of the Q-criterion, which is defined as the second invariant of the instantaneous velocity gradient tensor [45]. The iso-surfaces are used to identify and portray the turbulent coherent structures of the wake, which are inherently three-dimensional. The iso-surfaces are colored by the spanwise vorticity, ω_z, and demonstrate how the wake behavior changes as standard serrations are introduced then their geometrical parameters modified. For the case of a flat TE (C1.2), the wake is non-uniform and has almost no observable coherent structures, while serrated cases (C2.1, C2.2 and C2.3) are clearly subject to vortex shedding.

For the case of a flat TE (C1.2), the wake is turbulent but has no identifiable coherent structures. For the cases of standard serrations (C1.2, C2.2 and C2.3), the wake is characterized by sinusoidal vortex shedding. The amplitude and frequency of the observed phenomenon change as the serrations amplitude and wavelengths are varied. C2.1 is subject

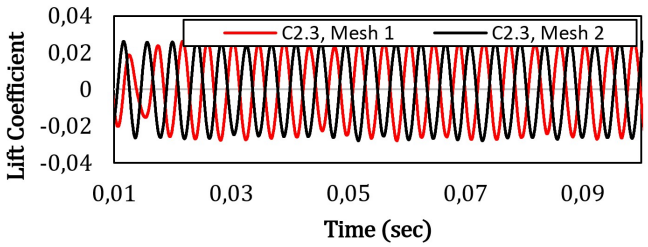

Figure 11: Lift-coefficient history of C2.3 using two different meshes.

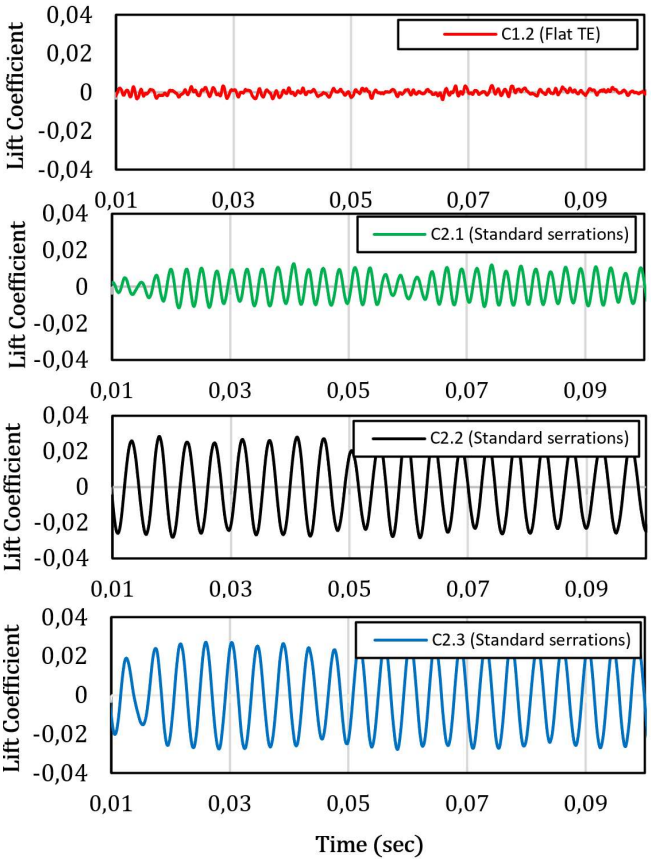

Figure 12: Lift-coefficient history for cases C1.2,C2.1,C2.2, and C2.3.

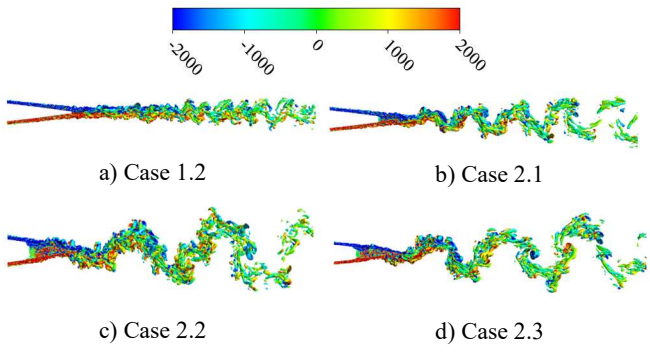

Figure 13: Instantaneous Q-Criterion colored by ω_z.

to the highest shedding frequency and the smallest amplitude. C2.2 and C2.3 are subject to similar vortex shedding amplitudes, but the frequency is higher in C2.3. The vortex

shedding frequency can also be approximated by counting the number of full periodic cycles in the airfoil wake and dividing it by the through-flow time (T_{TF}). Vortex shedding is caused by the interaction of two shear layers as they leave the airfoil surface. Because of the inherent instability of the turbulent boundary layer, alternating low pressure zones are generated downstream of the airfoil, giving rise to fluctuating forces acting normal to the wind direction, which in turn explains the sinusoidal lift coefficient variation (figure 12). The frequencies at which vortices are shed from the airfoil TEs are equal to those at which the non-dimensional lift forces acting on the airfoil vary, and can thus be accurately calculated by applying a discrete FFT on the lift-coefficient history plots. Then, cases C2.1, C2.2, C2.3 and C4 are subject to vortex shedding frequencies of 388 Hz, 218 Hz, 248 Hz, and 210, respectively. A generated vortex is initially growing and fed by circulation from the separated shear layer, until it becomes strong enough to roll up and draw the opposing shear layer across the wake. At that point, this vorticity of opposite sign interrupts any further supply of circulation to the growing vortex, which then stops increasing in strength. As a result, that vortex is shed and convected downstream while a new one of opposite vorticity takes its place and the cycle keeps going [46, 47]. As the serration amplitude ($2h$) is reduced, the root bluntness (ϵ) is also reduced and the shear layers are brought closer together. Subsequently, the interaction between the two shear layers is facilitated and the periodic time is shortened, giving rise to a higher vortex shedding frequency [47].

In order to study the dynamics of vortex shedding, the Strouhal number, $St = f_s L/u_\infty$, is often used [48], in which f_s is the vortex shedding frequency in Hz, L is the characteristic length separating the shear layers in meters, which is equal to ϵ, and u_∞ is the free-stream velocity. St represents the ratio of inertial forces due to the local acceleration of the flow to the inertial forces due to the convective acceleration. The first is a product of turbulence and how the velocity of a fluid particle changes due to the inherent instability of the TBL, while the latter is an indication of how much the velocity changes as the flow moves across the fluid domain. St is particularly helpful for flows characterized with periodic motion as it associates the oscillations of the flow due to the inertial forces to the changes in velocity due to the convective acceleration of the flow field. In the case of a flat TE, the oscillations are not prominent, seeing that they are swept by the fast-moving fluid (figure 13a). When changing the serration amplitude ($2h$) from 30 mm (C2.1) to 60 mm (C2.2), the observed vortex shedding frequency (figures 13b and 13d) is reduced and St increases ($St_{2.1} = 0.119$ and $St_{2.3} = 0.168$). Increasing λ while keeping $2h$ constant leads to an increase in vortex shedding frequency and St ($St_{2.2} = 0.148$ and $St_{2.3} = 0.168$). The observed trend is in good agreement with the work of Hu et al.[49], as well as the aforementioned findings. Different airfoils will have different root bluntness for the same serration amplitude depending on their profile, and subsequently different vortex shedding frequencies. Wake vorticity is also dissipated faster in cases C2.3 and C2.2 than C2.1 and C1.2, which can be seen by inspecting the vorticity magnitude in the wake, shown in figure 14. Lastly, figure 15 gives the streamwise vorticity, $\omega_x = \partial u_y/\partial z - \partial u_z/\partial y$, contours for all the simulated cases. The two limits of the contour correspond to fluid particles having equal vorticity but in opposite directions. For the case of a flat TE (C1.2), turbulent, counter-rotating coherent structures are observed at the TE. For the cases having standard serrations (C2.1, C2.2 and C2.3), the turbulent coherent structures are allowed to pass between the serrations, across the airfoil surface.

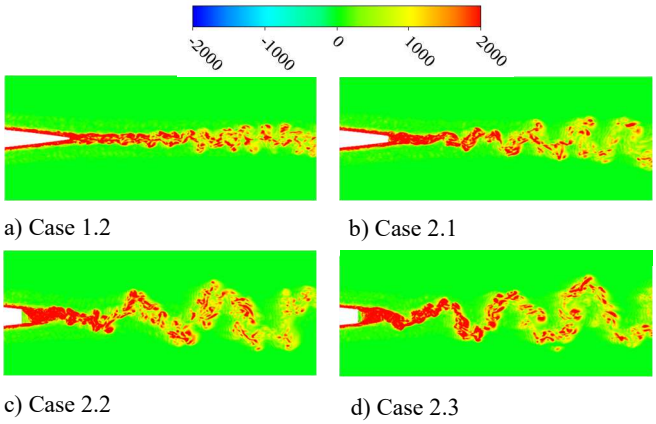

a) Case 1.2 b) Case 2.1

c) Case 2.2 d) Case 2.3

Figure 14: Instantaneous vorticity magnitude contours.

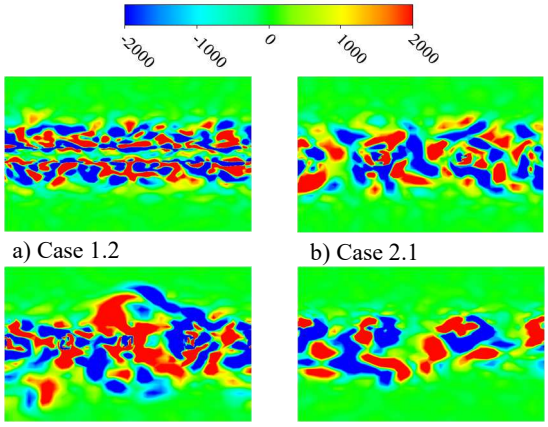

a) Case 1.2 b) Case 2.1

c) Case 2.2 d) Case 2.3

Figure 15: Instantaneous ω_x contours at $x/c = 1$.

4.3 Far field noise

The FW-H aeroacoustic analogy [30, 31] is used to compute the radiated far-field noise for the computational cases C1.2, C2.1, C2.3. In order to keep the computational cost reasonable, the span of the simulation domains is kept smaller than that of the experimental testing. Acoustic data is sampled every 2 flow-timesteps and data sampling is performed for $3T_{FT}$ after the flow is fully developed, resulting in a sampling frequency of 41.67 kHz and a frequency resolution of 28.4 Hz, where the frequency resolution is defined as the inverse of the sampling period. Pressure fluctuations are propagated to receivers placed midspan at a distance of 1.5 meters directly above the airfoils' TEs, as seen in figure 16. Cases C2.1, C2.2 and C2.3 show periodic

patterns, where the amplitude is highest in C2.2 and C2.3, and the periodic frequency is highest in C2.1. Discrete FFT is performed on the resulting time signals seen to compute the sound pressure level (SPL) signal in the frequency domain, as shown in figure 17. The Hanning window is applied to the time signal to reduce numerical leakages associated with the discrete FFT [50]. Case C1.2 only exhibits broadband behavior. Tonal peaks are observed for C2.1, C2.2 and C2.3 at 397 Hz, 198 Hz and 240 Hz, respectively. The tonal peak amplitudes are equal for C2.2 and C2.3. The peak amplitude is 3.3 dB lower in C2.1, meaning the tonal noise is louder for the cases having longer serrations. The narrowband peaks are fundamentally justified by the vortex shedding caused by the serration root bluntness discussed in subsection 4.2 [51]. Figure 18 presents the far-field spectra obtained from simulating design C2.3 using two meshes, as previously mentioned. Both simulations predict the same narrow-band tonal peak amplitude and frequency, as well as comparable broad-band behavior at frequencies higher than the tonal peak.

As part of the current study, and in addition to the numerical predictions, wind tunnel testing has been performed to measure the noise of a NACA0012 airfoil with a straight TE and a serrated sawtooth TE. The airfoil has a chord length c of 300 mm, and the width is similar to the width of the nozzle exit at 510 mm. The airfoil AOA is set to zero and fixed to the nozzle exit by two side plates. The microphone was placed at about 1.4 m from the TE at a polar angle of 90°. The free jet velocity was set to 24 m/s and the flow, parameters and chord length are similar to the computational cases, yielding a Re_c of approximately 500,000. The fluctuating pressure-time signals for the used microphone are recorded and then used to calculate the SPL spectrum. The data sampling frequency is set to 20 kHz and the data sampling period is 30 seconds, corresponding to a frequency resolution of 0.033 Hz. The obtained signal is also passed through a time-domain filter to remove the low and high frequency contamination, caused by the microphone's low frequency roll off and high-frequency aliasing. The band-pass filter used is a Butterworth filter with the first and second stopband frequencies of 100 and $f_s/2$ Hz respectively, where f_s is the sampling frequency. The sound pressure level, SPL, is computed using the root mean square (RMS) of filtered pressure signal using the following equation:

$$SPL = 10log_{10}\left(\frac{P_{RMS}^2}{P_{ref}^2}\right) \quad (23)$$

where P_{ref} is the standard reference pressure in air, 20 μPa. Figure 19 shows the turbulent broadband noise spectra (SPL) radiated by a straight TE and a serrated TE, respectively. Note that the serrated TE is a non-flat plate type where a certain degree of bluntness exists at each sawtooth root for all experimental and computational cases. Vortex shedding has been shown to be emanated from the blunt roots, which then proceeds to generate the tonal noise. A tonal peak is observed at 290 Hz in case E2 and broadband reduction occurs at frequencies higher than the tonal component (350 Hz to 5 kHz).

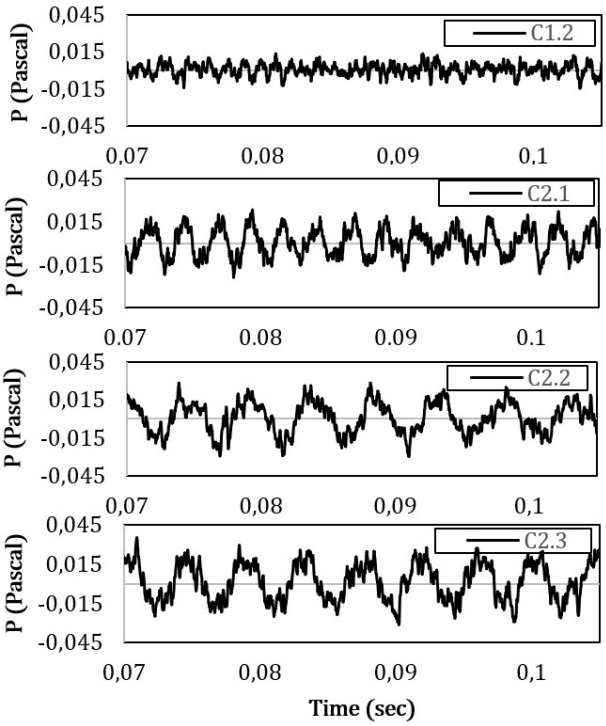

Figure 16: Time-domain noise signals propagated to receiver.

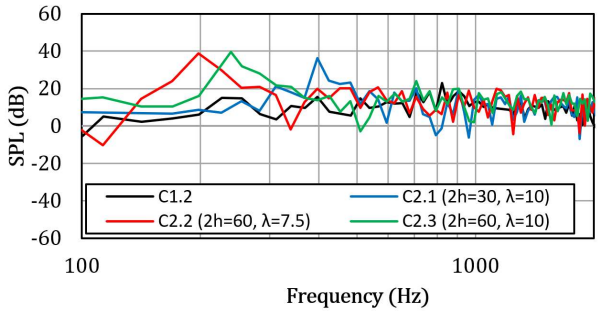

Figure 17: Frequency-domain noise signals of C1.2, C2.1, C2.2 and C2.3.

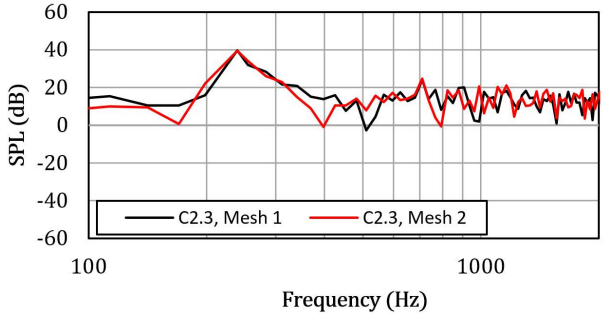

Figure 18: Frequency-domain noise signals of C2.3 using 2 meshes.

The numerical simulations and the wind tunnel experiments predict comparable acoustic behavior; by comparing C1.2 to E0 and C2.3 to E2, the numerically simulated and experimentally obtained SPL levels follow similar acoustic spectra shapes, but with different amplitude. This is mainly caused by limited computational domain span, compared to

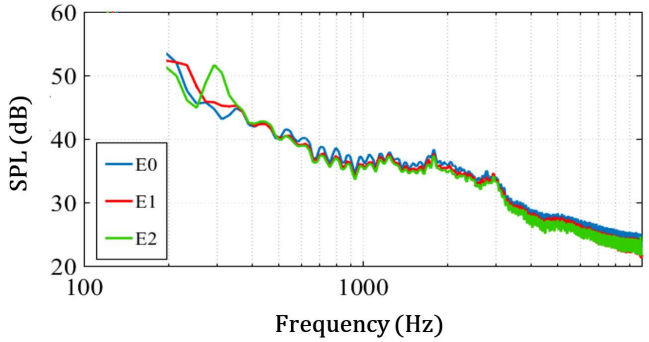

Figure 19: Experimentally obtained SPL.

the experimental one ($span_{ELES} = 30$ mm, compared to $span_{Experimental} = 500$ mm), and the noise source contribution of the airfoil leading edge, which is not accounted for in the used ELES configuration. Since the work is focused on TE noise, it is reasonable to neglect the noise radiated by other sections of the airfoil. Narrowband tonal peaks are predicted in both numerical and experimental far-field spectra for the case of sawtooth serrations having $2h = 60$ mm and $\lambda = 10$ mm (C2.3 and E2). The difference in the predicted tonal frequencies is consistent with the results of Kim et al.[22]. The difference in the tonal peak frequencies is attributed to the subtle differences that exist between the numerical and experimental geometric models and inflow conditions, such as turbulence, and the limited LES domain size.

Experimental results confirm that sawtooth serrations reduce the generated broadband noise at the expense of adding a narrow-band tonal peak, caused by vortex shedding associated with the bluntness of the serration roots. The broadband reduction was not captured in the numerical simulations. Increasing the sensitivity of the simulation would require a finer mesh and longer simulation time, which would render the simulations unfeasible. For the broadband reduction to be captured without significantly increasing the simulation run-time, more powerful computer clusters are required to allow for a larger LES domain and a higher frequency resolution (longer sampling period). The obtained accuracy is found to be satisfactory for the purposes discussed in this paper, when compared to the corresponding reduction in computing effort. ELES successfully predicted the narrowband tonal noise component at a relatively low computational cost, and was used to assess the effect of different serration parameters on the tonal peak and frequency.

5 Conclusion

Embedded Large Eddie Simulations as well as experimental wind tunnel testing are carried out for NACA0012 airfoils having different TE configurations. Different sawtooth serrations having various serration amplitudes and wavelengths were investigated for a freestream flow velocity $u_\infty = 24$ [, $AOA = 0$ and Re_c of approximately 500,000. A mesh convergence study is performed and the obtained pressure coefficient distribution is validated. Results show excellent agreement with experimental data and full LES predictions. The validated computational approach is employed to gain an improved understanding of the flow characteristics of serrated-TE airfoils, as well as predict any acoustic tones, while experimental testing is conducted to obtain highly accurate acoustic results.

The introduction of serrations is shown to strongly affect the flow field, mitigating the sharp TE discontinuity and improving mixture between the upper and lower sides of the airfoil. Serrations are shown to concentrate the maximum pressure fluctuation region to downstream of the serration roots. Due to the introduced bluntness of these non-flat plate type sawtooth serrations, vortices are shed from the serration roots, generating narrowband tonal peaks. Narrow-band tonal peaks are observed in the far-field noise spectra at 397 Hz, 198 Hz and 240 Hz for C2.1, C2.2 and C2.3, respectively. The tonal peak amplitudes are equal for C2.2 and C2.3, which share the same $2h = 60$ mm and $\epsilon = 16.3$ mm. The peak amplitude was lower in C2.1 by 3.3 dB, suggesting that the tonal noise is louder for cases having longer serrations and increased root bluntness. Longer serrations, and higher values of ϵ are responsible for the strength of the shed vortices and the intensity of the radiated tonal noise. The frequency at which the tonal peaks occur can be controlled for the same 2h and ϵ by modifying the wavelength, λ. Larger values of λ for the same $2h$ and ϵ lead to higher tonal peak frequencies, and larger values of ϵ for the same $2h$ and λ lead to lower tonal peak frequencies accompanied by higher peak amplitudes.

Experimental results confirm that sawtooth serrations reduce the broadband generated noise at the expense of adding a tonal peak. Qualitative comparisons are made between computational results and experimental measurements and satisfactory agreement is achieved. The numerical simulations and the wind tunnel experiments predict similar acoustic behavior and shape of the far-field noise spectra. In combination with the FW-H analogy, ELES successfully captures the narrowband peaks of the radiated far-field noise, which are associated with vortex shedding. The results of this investigation illustrate how ELES can be used as a reasonable alternative to the more computationally demanding full LES or direct numerical simulation approaches. Future work aims to utilize the aforementioned methods for the development of new noise-suppressing TE designs.

References

[1] Chapter 2: Effects of Noise Pollution on Birds: A Brief Review of Our Knowledge. Ornithol. Monogr. 2012, 74 (1), 6–22. doi: 10.1121/1.4784049

[2] Bronzaft, A. L. Noise Pollution: A Threat to Our Mental and Physical Well-being. J. Acoust. Soc. Am. 2004, 115 (5), 2567–2567. doi: 10.3390/wsf-00623

[3] Jianu, O.; Naterer, G.; Rosen, M. Noise Polution Prevention in Wind Turbines: Status and Recent Advances. In Proceedings of The 1st World Sustainability Forum; MDPI: Basel, Switzerland, 2011. dio: 10.3390/wsf-00623

[4] Graham, R. R. The Silent Flight of Owls. J. R. Aeronaut. Soc. 1934, 38 (286), 837–843.

[5] Lilley, G. A Study of the Silent Flight of the Owl. In 4th AIAA/CEAS Aeroacoustics Conference; American Institute of Aeronautics and Astronautics: Reston, Virigina, 1998. doi: 10.1017/s0368393100109915

[6] Herr, M.; Dobrzynski, W. Experimental Investigations in Low-Noise Trailing Edge Design. AIAA J. 2005, 43 (6), 1167–1175. doi: 10.2514/1.11101

[7] Gruber, M.; Joseph, P.; Azarpeyvand, M. An Experimental Investigation of Novel Trailing Edge Geometries on Airfoil Trailing Edge Noise Reduction. In 19th AIAA/CEAS Aeroacoustics Conference; American Institute of Aeronautics and Astronautics: Reston, Virginia, 2013. doi: 10.2514/6.2013-2011

[8] Chong, T. P.; Vathylakis, A.; Joseph, P. F.; Gruber, M. Self-Noise Produced by an Airfoil with Nonflat Plate Trailing-Edge Serrations. AIAA J. 2013, 51 (11), 2665–2677. doi: 10.2514/1.j052344

[9] Chen, E.; Ma, Y.; Yang, A.; Zhao, G. Experimental Investigation on Noise Emissions of an Airfoil with Non-Flat Plate Trailing Edge Serrations. J. Mech. Sci. Technol. 2019, 33 (7), 3069–3074. doi: 10.1007/s12206-019-0601-x

[10] Manoha, E.; Troff, B.; Sagaut, P. Trailing-Edge Noise Prediction Using Large-Eddy Simulation and Acoustic Analogy. AIAA J. 2000, 38 (4), 575–583. doi: 10.2514/2.1015

[11] Agrawal, B. R.; Sharma, A. Numerical Investigations of Bio-Inspired Blade Designs to Reduce Broadband Noise in Aircraft Engines and Wind Turbines. In 54th AIAA Aerospace Sciences Meeting; American Institute of Aeronautics and Astronautics: Reston, Virginia, 2016. doi: 10.2514/6.2016-0760

[12] Tang, H.; Lei, Y.; Fu, Y. Noise Reduction Mechanisms of an Airfoil with Trailing Edge Serrations at Low Mach Number. Appl. Sci. (Basel) 2019, 9 (18), 3784. doi: 10.3390/app9183784

[13] Zilstra, A.; Johnson, D. LES and FW-H Prediction of Aeroacoustic Noise for a SD 7037 Airfoil for Wind Turbine Applications. In 25th AIAA/CEAS Aeroacoustics Conference; American Institute of Aeronautics and Astronautics: Reston, Virginia, 2019. doi: 10.2514/6.2019-2537

[14] Rumpfkeil, M. P. Using Steady Flow Analysis for Noise Predictions. Comput. Fluids 2017, 154, 347–357. doi: 10.1016/j.compfluid.2017.03.003

[15] Hosder, S.; Schetz, J. A.; Mason, W. H.; Grossman, B.; Haftka, R. T. Computational-Fluid-Dynamics-Based Clean-Wing Aerodynamic Noise Model for Design. J. Aircr. 2010, 47 (3), 754–762. doi: 10.2514/1.29105

[16] Albarracin, C.; Doolan, C.; Jones, R.; Hansen, C.; Brooks, L.; Teubner, M. D. A RANS-Based Statistical Noise Model for Trailing Edge Noise. In 18th AIAA/CEAS Aeroacoustics Conference (33rd AIAA Aeroacoustics Conference); American Institute of Aeronautics and Astronautics: Reston, Virigina, 2012. doi: 10.2514/6.2012-2181

[17] Remmler, S.; Christophe, J.; Anthoine, J.; Moreau, S. Computation of Wall Pressure Spectra from Steady Flow Data for Noise Prediction. In 16th AIAA/CEAS Aeroacoustics Conference; American Institute of Aeronautics and Astronautics: Reston, Virigina, 2010. doi: 10.2514/6.2010-4000

[18] Quéméré, P.; Sagaut, P. Zonal Multi-Domain RANS/LES Simulations of Turbulent Flows: ZONAL RANS/LES SIMULATIONS. Int. J. Numer. Methods Fluids 2002, 40 (7), 903–925. doi: 10.1002/fld.381

[19] Terracol, M. A Zonal RANS/LES Approach for Noise Sources Prediction. Appl. Sci. Res. 2006, 77 (1–4), 161–184. doi: 10.1007/s10494-006-9042-6

[20] Fröhlich, J.; von Terzi, D. Hybrid LES/RANS Methods for the Simulation of Turbulent Flows. Prog. Aerosp. Sci. 2008, 44 (5), 349–377. doi: 10.1016/j.paerosci.2008.05.001

[21] Mathey, F. Aerodynamic Noise Simulation of the Flow Past an Airfoil Trailing-Edge Using a Hybrid Zonal RANS-LES. Comput. Fluids 2008, 37 (7), 836–843. doi: 10.1016/j.compfluid.2007.04.008

[22] Kim, T.; Jeon, M.; Lee, S.; Shin, H. Numerical Simulation of Flatback Airfoil Aerodynamic Noise. Renew. Energy 2014, 65, 192–201. doi: 10.1016/j.renene.2013.08.036

[23] Lane, G.; Croaker, P.; Ding, Y. Embedded Large Eddy Simulation Method for Predicting Flow-Induced Noise. Proceedings of ACOUSTICS. 2019.

[24] Zuo, Z. G.; Huang, Q.; Liu, S. An Analysis on the Flow Field Structures and the Aerodynamic Noise of Airfoils with Serrated Trailing Edges Based on Embedded Large Eddy Flow Simulations. J. Appl. Fluid Mech. 2019, 12 (2), 327–339. doi: 10.29252/jafm.12.02.29142

[25] ANSYS Fluent 2019 Theory Guide, ANSYS, Inc 2019

[26] Leonard, A. Energy Cascade in Large-Eddy Simulations of Turbulent Fluid Flows. In Turbulent Diffusion in Environmental Pollution, Proceedings of a Symposium held at Charlottesville; Elsevier, 1975; pp 237–248. doi: 10.1016/s0065-2687(08)60464-1

[27] Hinze, J. O. Turbulence, 2nd ed.; McGraw-Hill: New York, NY, 1976.

[28] Nicoud, F.; Ducros, F. Embedded Large Eddy Simulation Method for Predicting FlowInduced Noise. Flow, Turbulence and Combustion 62, 183–20, 1999. https://doi.org/10.1023/A:1009995426001

[29] Mathey, F.; Cokljat, D.; Bertoglio, J; Sergent, E. Specification of LES Inlet Boundary Conditions Using Vortex Method. Progress in Computational Fluid Dynamics, vol. 6, 2006. https://doi.org/10.1142/s0219887821501644.

[30] Lighthill, M. J. On Sound Generated Aerodynamically I. General Theory. Proc. R. Soc. Lond. 1952, 211 (1107), 564–587. doi: 10.1098/rspa.1952.0060

[31] Williams, J. E. F.; Hawkings, D. L. Sound Generation by Turbulence and Surfaces in Arbitrary Motion. Philos. trans. R. Soc. Lond. 1969, 264 (1151), 321–342. doi: 10.1098/rsta.1969.0031

[32] Brentner, K. S.; Farassat, F. Analytical Comparison of the Acoustic Analogy and Kirchhoff Formulation for Moving Surfaces. AIAA J. 1998, 36 (8), 1379–1386. doi: 10.2514/2.558

[33] Berger, M.; Aftosmis, M. Progress towards a Cartesian Cut-Cell Method for Viscous Compressible Flow. In 50th AIAA Aerospace Sciences Meeting including the New Horizons Forum and Aerospace Exposition; American Institute of Aeronautics and Astronautics: Reston, Virigina, 2012. doi: 10.2514/6.2012-1301

[34] Ghmati, R. E.; Jawad, B. A.; Koutsavdis, E. An Investigation of CutCell Meshing Strategies for Accurate Aerodynamic Performance Prediction. SAE Int. J. Passeng. Cars - Mech. Syst. 2012, 5 (1), 369–380. doi: 10.4271/2012-01-0499

[35] ANSYS Fluent 2019 User Guide, ANSYS, Inc 2019

[36] Menter, F. R., "Best Practice: Scale-Resolving Simulations in ANSYS CFD," 2015, ANSYS Germany GmbH

[37] Menter, F. R. Two-Equation Eddy-Viscosity Turbulence Models for Engineering Applications. AIAA J. 1994, 32 (8), 1598–1605. doi: 10.2514/3.12149

[38] Al Tlua, B., and Rocha, J., “Development and Testing of an Aeroacoustic Wind Tunnel Test Section,” Canadian Acoustics, vol. 47, 2019.

[39] Al Tlua, B., and Rocha, J., "Optimization and Testing of Flat-Plate Trailing-Edge Serration Geometry for Reducing Airfoil Self-Noise," Canadian Acoustics, vol. 48, 2020.

[40] Clauser, F. H. Turbulent Boundary Layers in Adverse Pressure Gradients. J. Aeronaut. Sci. (Inst. Aeronaut. Sci.) 1954, 21 (2), 91–108.

[41] Falkner, V. M., and Skan, W. Some approximate solutions of the boundary layer equations. A.R.C Reports and Memoranda, 1930, no. 1314.

[42] Ludwieg, H., and Tillmznn, W. Investigations of the wall shearing stress in turbulent boundary layers. NACA T.M., 1950, no. 1285.

[43] Lee, H.; Kang, S.-H. Flow Characteristics of Transitional Boundary Layers on an Airfoil in Wakes. J. Fluids Eng. 2000, 122 (3), 522–532. doi: 10.1115/1.1287592

[44] Marsden, O.; Bogey, C.; Bailly, C. Direct Noise Computation around a 3-D NACA 0012 Airfoil. In 12th AIAA/CEAS Aeroacoustics Conference (27th AIAA Aeroacoustics Conference); American Institute of Aeronautics and Astronautics: Reston, Virigina, 2006. doi: 10.2514/6.2006-2503

[45] Chong, M. S.; Perry, A. E.; Cantwell, B. J. A General Classification of Three-dimensional Flow Fields. Phys. Fluids 1990, 2 (5), 765–777.

[46] Green, R. B.; Gerrard, J. H. Vorticity Measurements in the near Wake of a Circular Cylinder at Low Reynolds Numbers. J. Fluid Mech. 1993, 246 (1), 675–691. doi: 10.1017/s002211209300031x

[47] Gerrard, J. H. The Mechanics of the Formation Region of Vortices behind Bluff Bodies. J. Fluid Mech. 1966, 25 (2), 401–413. doi: 10.1017/s0022112066001721

[48] Blevins, R. D., Flow-induced vibration, Malabar (Fl.): Krieger publ., 2001.

[49] Hu, J.; Wang, Z.; Zhao, W.; Sun, S.; Sun, C.; Guo, C. Numerical Simulation on Vortex Shedding from a Hydrofoil in Steady Flow. J. Mar. Sci. Eng. 2020, 8 (3), 195. doi: 10.3390/jmse8030195

[50] William H. Press; Teukolsky, S. A.; Vetterling, W. T.; Flannery, B. P. Numerical Recipes; Cambridge University Press: Cambridge, England, 1986.

[51] Strouhal, Vincenz. Über eine besondere Art der Tonerregung. Stahel, 1878.